Domain structure analysis of $Pb(Zn_{1/3}Nb_{2/3})O_3$-9%$PbTiO_3$ single crystals using optical second harmonic generation microscopy

Junichi Kaneshiro* and Yoshiaki Uesu†
Department of Physics, Waseda University, 3-4-1 Okubo, Shinjuku, Tokyo 169-8555, Japan
(Received 1 August 2010; revised manuscript received 3 November 2010; published 22 November 2010)

The domain structures of relaxor-ferroelectric $Pb(Zn_{1/3}Nb_{2/3})O_3$-9%$PbTiO_3$ (PZN-9PT) single crystals with a morphotropic phase boundary (MPB) composition are observed with a scanning second harmonic generation (SHG) microscope. Three-dimensional domain structures are obtained from sectional SH images along the axial direction. The domain structures are explained well by the strain compatibility theory that is based on the ferroelectric/ferroelastic phase transition of $m\bar{3}mFm(p)$ with the monoclinic space group *Pm*. The SHG images are divided into several parts, and the light-polarization dependence (PolD) at each site is calculated by minimizing the least-squares errors of the nonlinear susceptibilities. The PolDs are fitted well by theoretical formulas of the SH intensities for the *Pm* symmetry, and the two-dimensional map of the PolD coincides well with the corresponding SHG image of the domain structures. The monoclinic *Pm* symmetry at the MPB of PZN-9PT is determined at the optical diffraction limit of 460 nm.

DOI: 10.1103/PhysRevB.82.184116 PACS number(s): 77.80.Jk, 77.84.−s, 77.80.Dj, 42.65.−k

I. INTRODUCTION

Large dielectric, piezoelectric, and elastic responses are expected as a result of heterophase fluctuations in materials.[1] Typical examples are relaxors in which polar nanoregions (PNRs) appear in the cubic matrix at temperatures several hundred Kelvin above the dielectric peak temperature.[2] The formation of PNRs causes large, broad, and strongly frequency-dependent dielectric susceptibility. High piezoelectric constants and mechanical coupling coefficients are observed in solid solutions of relaxors and ferroelectrics at specific composition ratios. This compositional phase boundary is termed as the morphotropic phase boundary (MPB). The symmetry of the MPB has been found to be lower than those of the two end members by using polarization microscopy[3] and x-ray diffraction methods.[4] An *ab initio* calculation also shows that symmetry lowering to the monoclinic phase makes the rotation of $\mathbf{P}_s$ more facile, which induces greater piezoelectricity.[5] Associated with the phase transition from the cubic to the monoclinic phase, 24 types of domains with different orientations of spontaneous polarization and 42 types of domain boundaries are predicted by the strain compatibility theory.[6] When a domain state is regarded as a material phase, the heterophase fluctuations due to the domain reconfiguration can lead to large susceptibilities. Therefore, the observation of domain structures at the MPB is essential, and certain researches with optical, x-ray, neutron, transmission electron microscopy, and atomic force microscopy techniques have been performed. For $Pb(Zn_{1/3}Nb_{2/3})O_3$-x%$PbTiO_3$ (PZN-xPT), the symmetry of its MPB has not been determined. Some authors claim that the symmetry of the MPB is monoclinic,[7–9] whereas others provide evidence that it is rhombohedral with either microtwins or nanotwins[10] or tetragonal with microtwins or nanotwins.[11] Even limited to optical observations, a disagreement exists in samples with a small difference of x: with $x=8\%$, the symmetry is reported to be rhombohedral,[12] while with $x=9\%$ it is monoclinic[3,9] or mixture of rhombohedral and tetragonal.[13,14] In this situation, the precise investigation by diffraction techniques is prerequisite on the same sample for optical observations. In this study, we used the same PZN-9PT samples as were used in neutron-scattering experiments.[7,8] The analyses of them determined the symmetry of the samples to be on the Mc line of the space group *Pm*.

The present paper reports the two-dimensional (2D) and three-dimensional (3D) observations of the domain structures in PZN-9PT using a scanning second harmonic generation (SHG) microscope at the spatial resolution of the optical diffraction limit, and the symmetry is determined by analyzing the observed 3D SHG images and the 2D maps of the light-polarization diagram [polarization dependence (PolD)] on the basis of the strain compatibility theory.[15]

It should be stressed that the SHG is quite a sensitive phenomenon to the change in spontaneous polarization of ferroelectrics, making it a suitable tool for observing domain structures.[16,17] It should also be noted that the SHG microscopic observations are dominated by the diffraction limit similar to other far-field optical methods. Therefore, SHG images provide the macroscopic symmetry averaged over local heterogeneous structures[18] with the optical resolution.

Section II describes the experimental conditions, i.e., the dimension and orientation of the specimens as well as the optical setup of the SHG microscope. Section III shows the 3D observations of domain structures and the 2D PolD maps. Section IV explains the analyses using the strain compatibility theory. Section V is the conclusion. The matrices for the polar third-rank susceptibilities (SHG constants) of the 12 possible domains in *Pm* are summarized in the Appendix.

II. EXPERIMENTAL CONDITIONS

A. PZN-9PT samples

Single crystals of PZN-9PT were grown by the flux method. This composition ratio is located in the middle of the MPB region as shown in Fig. 1(a).[19] Two flat plates are cut out perpendicular to the $[010]_c$ (c indicates the cubic

 ©2010 The American Physical Society

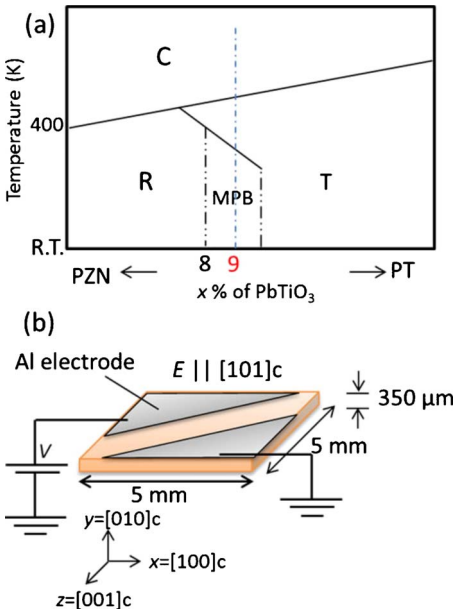

FIG. 1. (Color online) (a) The phase diagram of PZN-xPT mixed system (Ref. 19). PZN-9PT samples used in the present experiment are indicated with the dotted line. (b) A schematic illustration of the sizes and orientations of the sample and electrodes deposited on the sample. An electric field is applied along the $[101]_c$ direction.

axis) direction with a size of $5\times5\times0.35$ mm^3 after checking the orientation by x-ray diffraction and polished with alumina films and alumina powders. A surface roughness of less than 1 μm is obtained. Internal strains caused by the cut and polishing process are removed by annealing the samples at 500 °C for 6 h in the ambient atmosphere. For one of the annealed plates, aluminum electrodes are deposited by vacuum evaporation and a dc electric field of 5 kV/cm is applied along the $[101]_c$ direction during the cooling process from 60 °C to RT as illustrated in Fig. 1(b). Fractional domains reappeared after removing the electric field at RT. The two samples with and without the electric filed treatment are termed the poled and nonpoled samples, respectively.

B. Optical system for the scanning SHG microscope

The precise optical setup of the SHG microscope is described in Ref. 20 which can be used also as the SHG interference microscope. The present setup uses a part of it. The light source for generating SH waves in the sample is an Nd:YVO_4 pulsed laser with a wavelength of 1.064 μm, a 10 ns pulse width, and a 40 kHz repetition rate. The beam spread angle and the diameter are adjusted in two lenses and the fundamental light intensity is controlled by an attenuator composed of a half wave plate and a thin-film polarizer. A linearly polarized wave with small ellipticity of 10^{-5} is obtained with a second polarizer located behind the attenuator, and the light-polarization direction is changed by a half wave plate. A pair of objective lenses with a numerical aperture of 0.7, magnification of 100, 2 mm focal length, and a 10 mm working distance is used to form the quasiconfocal system. The lateral spatial resolution is estimated to be 0.46 μm from the optical diffraction limit and the axial resolution to be 3.1 μm based on the Rayleigh length of the incident laser beam and the refractive index of PZN-9PT.[21] Transmitted fundamental waves are removed with a filter, and only SH waves with a wavelength of 532 nm are detected by the photomultiplier tube after passing through an analyzer, a pinhole, and a spectrometer. The sample stage is positioned with a stepping motor for the scanning along the axial direction and for the in-plane wide scanning (150×150 μm^2 $<$scanning area $A<1\times1$ cm^2), while the stage is driven by a piezoactuator for the in-plane fine scanning ($A<150\times150$ μm^2).

C. Experimental procedures

Two-dimensional observations of the bottom surface are performed on the nonpoled sample. First, a wide area of 1500×1500 μm^2 is observed with a scanning step of 4 μm. Then, two small areas, area-1 (50×50 μm^2) and area-2 (100×100 μm^2), are selected, and fine SHG images of these areas are taken. For quantitative analyses, 2D maps of the PolD are measured for each area under the condition that the polarization directions of the incident and SH waves are kept parallel to each other. For the poled sample, 3D sectional observations from the bottom to the top surfaces are acquired. In addition, PolDs are also examined in the same procedure as described above.

III. EXPERIMENTAL RESULTS

A. Nonpoled sample

An SHG image of the PZN-9PT $(010)_c$ plate obtained by the wide scanning mode is shown in Fig. 2(a). The bright and dark parts represent the area generating strong and weak SH intensities, respectively. For comparison, a photograph of the same area taken by the polarization microscope with an incandescent light source and a sensitive color plate in the crossed Nicols is also shown in Fig. 2(b). The axes x, y, and z indicate the $[100]_c$, $[010]_c$, and $[001]_c$ directions, respectively. Domain structures with domain boundary directions satisfying $x\pm z=0$ are clearly observed in both figures.

Figures 3(a) and 3(b) show the SHG images of area-1 in Fig. 2(a) taken with a scanning step of 0.2 μm and the light-polarization angles $\theta=0°$ and 90°. Figure 3(c) shows the PolD map corresponding to Fig. 3(a). A calculated PolD for area-1 obtained from the theoretical formulas described in Sec. IV is shown in Fig. 3(d). The experimental results are in good agreement with the theoretical values. Figures 4(a) and 4(b) show the result for area-2 in Fig. 2(a). The corresponding PolD map is shown in Fig. 4(c). In this figure, the experimental and fitting results are plotted with the solid circles and lines, respectively. In Figs. 4(d) and 4(e), the calculated results obtained from the theoretical formulas for two 90° domains are shown in the polar diagram. The detailed analyses of Figs. 3 and 4 are given in Sec. IV.

B. Poled sample

An SHG image of the 3D domain structure of the PZN-9PT $(010)_c$ plate and typical PolDs at three sites are shown in

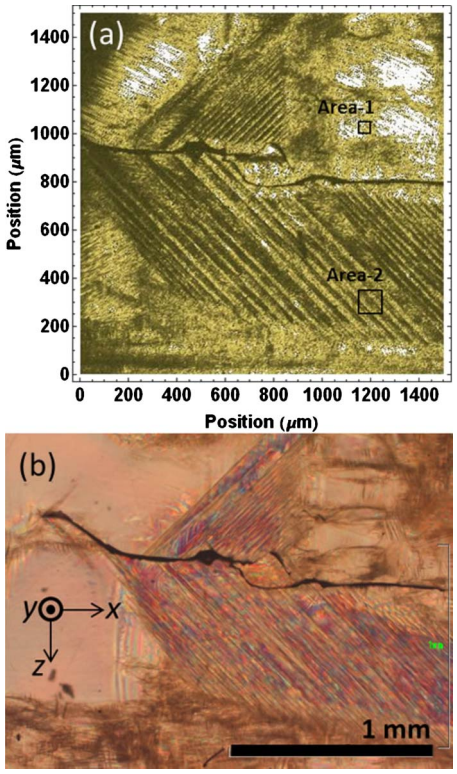

FIG. 2. (Color online) (a) SHG microscope image of the non-poled PZN-9PT sample taken at RT. (b) Polarization microscope image of the same part of (a).

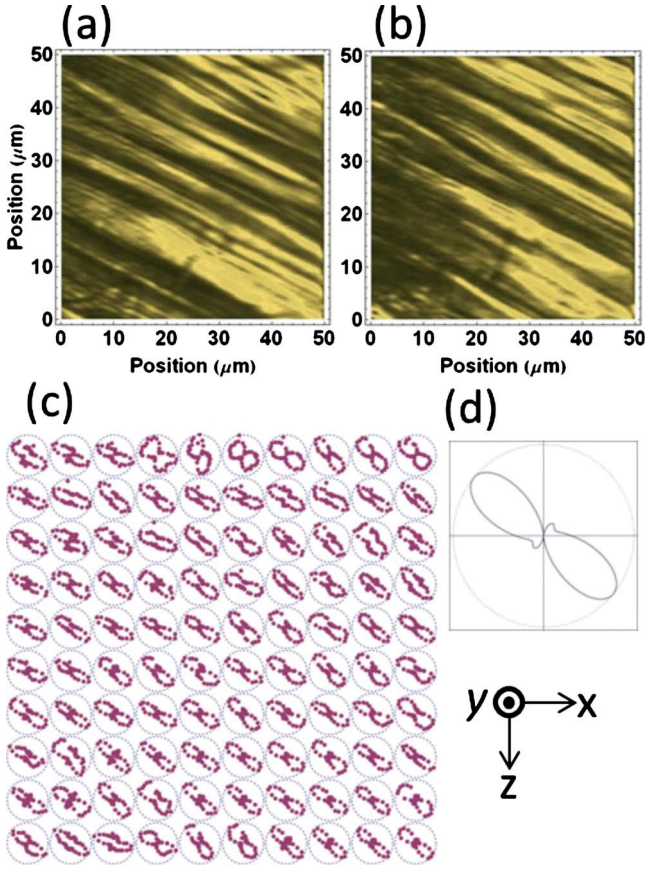

FIG. 3. (Color online) SHG images of area-1 with a light-polarization direction of (a) 0° and (b) 90°. (c) 2D map of the PolD in area-1. (d) The calculated PolD using the expected values from the fitting parameters.

Fig. 5. The intensity distributions of the xy cross section at $z=50$ μm and the yz cross section at $x=50$ μm are shown in Figs. 5(b) and 5(c), respectively. The necessary condition for observing 3D images by SHG is that the sign of the wave-number offset between the fundamental and SH waves should be negative.[20,22] However, the optical arrangement in the present study does not satisfy this condition because the polarization directions of the fundamental and SH waves are the same and parallel to the x axis. Therefore, the SH intensities at the bottom and top surfaces are much stronger than those from the inner region. Nevertheless, oblique lines are observed inside the sample as shown in Figs. 5(b) and 5(c). These images show that a near-single domain structure is obtained by the electric poling. The bright plane in Fig. 5(a), as well as the lines in Figs. 5(b) and 5(c), indicates an existence of a thin plate domain with a $\mathbf{P}_s$ different from the other region. The directions of the two lines in Figs. 5(b) and 5(c) are inclined by 45° and 22° from the x and z axes, respectively. Figures 5(d)–5(f) are the PolDs measured at the bottom surface, inside the domain, and the top surface. Only the PolD shown in Fig. 5(e) is apparently different from the others. The results are further discussed in Sec. IV.

IV. DISCUSSIONS

The symmetry of PZN-9PT at RT was determined to be monoclinic Pm by neutron-scattering experiments.[7,8] The structural sequence $m\bar{3}mFm(p)$ is a ferroelastic/ferroelectric phase transition, and the orientations of the domain boundaries follow Sapriel's theory,[15] which is derived from Curie's principle and the compatibility of spontaneous strains. Two possible directions, $\mathbf{P}_i$ and $\mathbf{P}_j$, are separated by a ferroelastic domain wall and are readily obtained from the relation between the strain tensor and the spontaneous polarization $\mathbf{P}_s$, which is expressed $(\mathbf{P}_i,\mathbf{P}_j)$. For $m\bar{3}mFm(p)$, 24 types of spontaneous polarization vectors and 12 types of ferroelastic strain tensors are possible. Let us consider the case where $\mathbf{P}_1=(p_1,0,p_3)$ with $p_3>p_1>0$. The Cartesian coordinates $x=[100]_c$, $y=[010]_c$, and $z=[001]_c$ are used. Then the corresponding spontaneous strain tensor S_1 is defined as

$$S_1=\begin{pmatrix} e_1 & 0 & e_5 \\ 0 & e_2 & 0 \\ e_5 & 0 & e_3 \end{pmatrix}, \tag{1}$$

where e_1, e_2, e_3, and e_5 depend on the lattice constants a, b, c and the axial angle β and are expressed in Eq. (2) with $t=(a+b+c)/3$ as[23]

$$e_1=\frac{a-t}{t},\quad e_2=\frac{b-t}{t},\quad e_3=\frac{c-t}{t},\quad e_5=\frac{1}{2}\left(\frac{\pi}{2}-\beta\right). \tag{2}$$

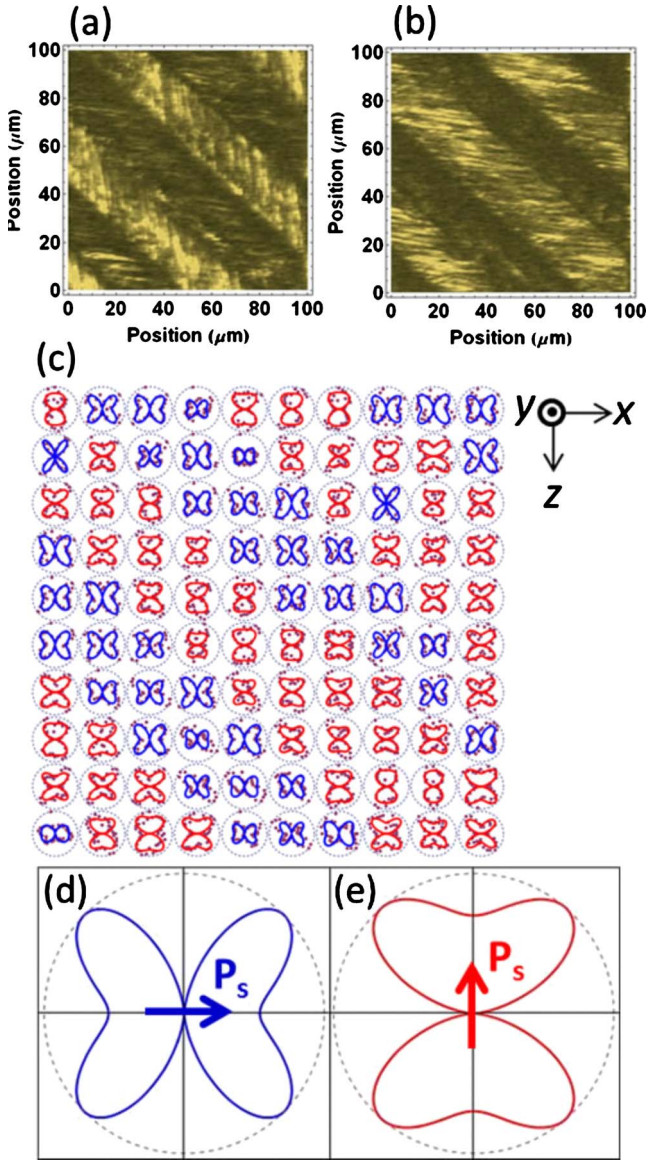

FIG. 4. (Color online) (a) SHG image of area-2 with a light-polarization direction of (a) 0° and (b) 90°. (c) 2D map of the PolD in the area-2. The blue and red lines are the fitting curves using Eqs. (4) and (5), respectively. (d) and (e) are the corresponding theoretical curves using the expected values of the fitting parameters. Arrows indicate the directions of $\mathbf{P}_s$ projected onto the observed zx plane.

Neutron scattering experiment determined these constants to be $e_1 \approx 0.001\,57$, $e_2 \approx -0.004\,37$, $e_3 \approx 0.002\,80$, and $e_5 \approx -0.000\,960$ at RT.[7] Other possible spontaneous polarization vectors and the corresponding strain tensors can be derived by using the symmetry elements which vanish at the cubic to monoclinic phase transition. In Table I, all possible $\mathbf{P}_s$'s are listed. Forty-two types of ferroelastic domain boundary orientations are obtained on the basis of strain compatibility. To explain the experimentally determined PolDs, the corresponding SHG tensors are calculated and are shown in the Appendix.

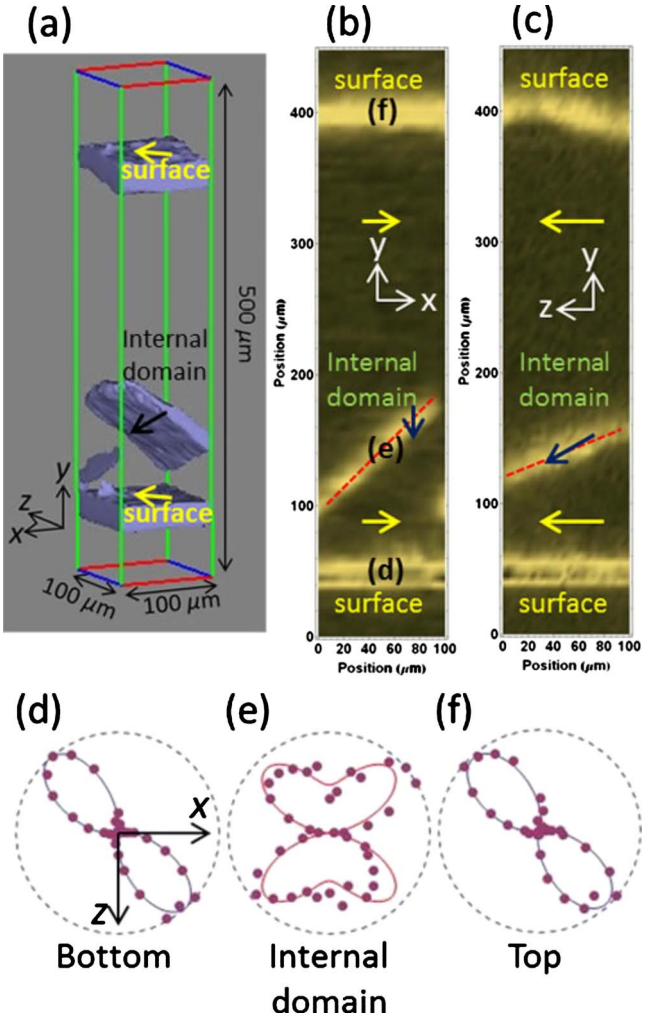

FIG. 5. (Color online) (a) 3D SHG image of the domain structure of the poled sample. (b) The xy cross-sectional image at $z=50$ μm. (c) The yz cross-sectional image at $x=50$ μm. PolDs are measured at (d) the bottom surface, (e) inside the sample, and (f) at the top surface.

A. Theoretical description of the polarization dependences of the SH intensities

The SH intensities produced in the zx plane are expressed as a function of the polarization angle θ under the condition of the parallel P (the polarization direction of the fundamental waves) and A (the polarization direction of the SH waves),

TABLE I. Possible spontaneous polarization vectors of PZN-9PT in monoclinic Pm.

Type 1	$\pm\mathbf{P}_1=(\pm p_1,0,\pm p_3)$	$\pm\mathbf{P}_2=(\pm p_3,0,\pm p_1)$
	$\pm\mathbf{P}_3=(\pm p_3,0,\mp p_1)$	$\pm\mathbf{P}_4=(\mp p_1,0,\pm p_3)$
Type 2	$\pm\mathbf{P}_5=(\pm p_1,\mp p_3,0)$	$\pm\mathbf{P}_6=(\pm p_3,\mp p_1,0)$
	$\pm\mathbf{P}_7=(\pm p_3,\pm p_1,0)$	$\pm\mathbf{P}_8=(\pm p_1,\pm p_3,0)$
Type 3	$\pm\mathbf{P}_9=(0,\pm p_3,\mp p_1)$	$\pm\mathbf{P}_{10}=(0,\mp p_3,\mp p_1)$
	$\pm\mathbf{P}_{11}=(0,\pm p_1,\pm p_3)$	$\pm\mathbf{P}_{12}=(0,\mp p_1,\pm p_3)$

$$\text{type 1: } I_1^{2\omega}(\theta) \propto [(\chi_{xxx}\cos^2\theta + \chi_{xzz}\sin^2\theta + 2\chi_{xzx}\sin\theta\cos\theta)\cos\theta + (\chi_{zxx}\cos^2\theta + \chi_{zzz}\sin^2\theta + 2\chi_{zzx}\sin\theta\cos\theta)\sin\theta]^2, \quad (3)$$

$$\text{type 2: } I_2^{2\omega}(\theta) \propto [(\chi_{xxx}\cos^2\theta + \chi_{xzz}\sin^2\theta)\cos\theta + 2\chi_{zzx}\cos\theta\sin^2\theta]^2, \quad (4)$$

$$\text{type 3: } I_3^{2\omega}(\theta) \propto [2\chi_{xzx}\cos^2\theta\sin\theta + (\chi_{zxx}\cos^2\theta + \chi_{zzz}\sin^2\theta)\sin\theta]^2. \quad (5)$$

For the 24 spontaneous polarization states, the observed PolDs are classified into three groups, expressed by Eqs. (3)–(5). Types 1–3 correspond to the classification in Table I, and the form of PolD is determined by the direction of $\mathbf{P}_s$ projected onto the zx plane. It should be noted that the PolD cannot distinguish antiparallel domains without the interference technique.[24,25]

B. Domain structure analyses

1. Nonpoled sample

Figures 3(a) and 3(b) show the SHG images of area-1 taken with θ=0° and 90°, respectively. No significant differences are observed between the two images. Figure 3(c) shows the PolD map of area-1. All PolDs are similar, indicating that only 180° domain structures exist in area-1. The elongated platelike regions with the bright and dark contrasts in Figs. 3(a) and 3(b) are not 180° domain structures but are the interference pattern from SH waves with opposite signs that are generated at the domain boundaries.[26] The elongation direction of these plates provides the direction of the 180° domain boundary and thereby the direction of $\mathbf{P}_s$. In Fig. 3, $+\mathbf{P}_2$ and $-\mathbf{P}_2$ satisfy this condition and the $\mathbf{P}_s$ direction is estimated to be inclined by approximately 27° from the z axis. This result agrees with the monoclinic Pm symmetry obtained by the neutron-scattering experiment.[8] In the case of x=8%, the result is more complicated: the phase is located on the Ma line under a weak electric field but changes to Mc with stronger field.[27] Because $\mathbf{P}_s$ is lying in the zx plane, Eq. (3) is used for the theoretical fitting of the PolDs for area-1. Figure 3(d) shows the average theoretical curve calculated with the expected values of the effective SHG coefficients that are obtained in the fitting process.

Figure 4(a) shows an SHG image of area-2. Seven domains with the boundaries along the $x-z$=0 are clearly observed. The intensity contrast is reversed when the light-polarization direction is rotated by 90° [Fig. 4(b)]. In the bright domains, platelike patterns similar to Fig. 3 are observed. The elongated direction of these patterns is almost parallel to the x or z axes. The fitted curves in Fig. 4(c) are obtained by the least-squares method. To calculate these curves, Eqs. (4) and (5) can be applied, and the equation which gives the smaller least-squares errors is adopted for each PolD. Then, a similar calculation to Fig. 3(d) is performed to determine the optimum fitting parameters. This process finally gives two PolDs, as shown in Figs. 4(d) and 4(e). The theoretical curves adequately explain the experimental results. The direction of arrows indicates the projection of $\mathbf{P}_s$ onto the zx plane. Therefore, the stripe direction in Figs. 4(a) and 4(b) is perpendicular to the $\mathbf{P}_s$ direction, which is contrary to the case of Fig. 3. This relation can be explained not by the tetragonal but by the monoclinic symmetry. This fact can be uniquely revealed by the combined analyses of the SHG images and PolD mapping.

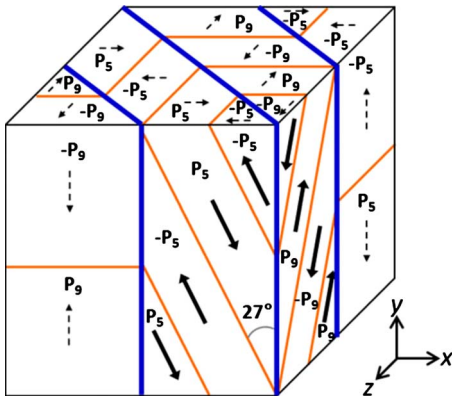

FIG. 6. (Color online) Schematic diagram of domain structures of area-2 (Fig. 5) in PZN-9PT formed with the combination of $(\mathbf{P}_5,\mathbf{P}_9)$. The solid lines indicate the $\mathbf{P}_s$ directions and the dotted lines indicate the projected orientations of 180° $\mathbf{P}_s$.

More precise analyses with the assumption of uncharged domain boundaries give four possible domain boundaries with $(\mathbf{P}_5,\mathbf{P}_9)$, $(\mathbf{P}_6,-\mathbf{P}_{12})$, $(\mathbf{P}_7,-\mathbf{P}_{11})$, and $(\mathbf{P}_8,\mathbf{P}_{10})$. The boundary directions are expressed as

$$x - z = 0. \quad (6)$$

Equation (6) represents the crystallographically prominent plane (W_f plane). The result of Fig. 4 can be interpreted also by the orthorhombic symmetry.[19,28–30] However, the orthorhombic phase is located at the end of the Mc line and is included as a special case of the monoclinic Pm. Actually its appearance depends strongly on the sample preparation condition and prehistory. Among four $\mathbf{P}_s$ combinations of the adjacent domains, the domain structure obtained with $(\mathbf{P}_5,\mathbf{P}_9)$ is shown in Fig. 6. The direction of $\mathbf{P}_s$ which is inclined by 27° from the cubic axis is shown in the solid arrows. Domain boundaries indicated by blue solid lines are parallel to the y axis, and inside these domains there exist 180° domain boundaries separated by $\pm\mathbf{P}_5$ or $\pm\mathbf{P}_9$, which are indicated by orange solid lines. The SHG image of area-1 coincides with the domain structure viewed along the xy plane.

The small local deviation of the PolD patterns in Figs. 3(c) and 4(c) is originated from the artifact due to small averaging number of the area which is almost comparable to the special resolution of the present experiment. The average over wider area would give PolD with less fluctuation. The fitting parameters obtained from Figs. 3(d), 4(d), and 4(e) are tabulated in Table II where χ_{ij} includes both SHG constant d_{ij} and corresponding interference term of PZN-9PT as a

TABLE II. Fitting parameters of the PolDs.

χ_{12}/χ_{11}	χ_{26}/χ_{11}	χ_{11}/χ_{33}	χ_{13}/χ_{33}	χ_{15}/χ_{33}	χ_{31}/χ_{33}	χ_{35}/χ_{33}
0.82 ± 0.07	0.89 ± 0.09	-0.19	0.97	-0.03	1.56	-1.21

function of Δk, sample thickness L, and the Rayleigh length z_0, which cannot be separated in the present procedure.

2. Poled sample

As mentioned in Sec. III B, the horizontal lines at $y=50$ μm and $y=400$ μm in Figs. 5(b) and 5(c) represent the specimen surfaces. The bright region inside the sample is not a domain boundary but a domain with thickness less than the axial resolution because the PolD [Fig. 5(e)] of this part is different from those at the bottom and top surfaces [Figs. 5(d) and 5(f)]. The inclination angles of the internal oblique lines are 45° from the x axis in the xy plane (b) and 22° from the z axis in the yz plane (c). The experimentally determined boundary orientation is expressed as

$$x - y - (\tan 22°)z = 0. \tag{7}$$

This type of boundary plane can be explained neither by the tetragonal nor rhombohedral symmetry but can be explained by the monoclinic symmetry. This experimental result confirms the monoclinic symmetry of PZN-9PT at the MPB.

The expression for the boundary plane [Eq. (7)] agrees with the theoretical calculation for $(\mathbf{P}_1, \mathbf{P}_{12})$, the boundary of which is expressed as $x-y-(\tan 18°)z=0$. As is similar to the area-2 in Fig. 4, the domain structure in Fig. 5 can also be interpreted by the orthorhombic symmetry. However, as described in Sec. IV B 2, this discussion would not be essential for the MPB symmetry and related physical properties.

C. Comparison of the domain structures of PZN-9PT and PMN-*x*PT

The domain structure of $Pb(Mg_{1/3}Nb_{2/3})O_3$-33%$PbTiO_3$ (PMN-33PT) with a MPB composition was precisely observed by a polarization microscope and analyzed by the strain compatibility theory.[6] The macroscopic symmetry of this compound was determined to be monoclinic Pm as PZN-9PT. The comparison of both compounds with the MPB composition indicates that the number of domain boundaries is same in both cases because the phase transition belongs to $m\bar{3}mFm(p)$. On the other hand, quantitative difference exists in the orientations of the S planes[6] as a result of different spontaneous strains and $\mathbf{P}_s$ orientations. In the case of PMN-33PT, the $\mathbf{P}_s$ direction is oriented 18° from the cubic axis,[8] while 27° in PZN-9PT. Concerning with nonprominent boundaries which are determined by the spontaneous strains, the present study reveals that similar boundaries to S_1 in PMN-33PT are observed in the poled sample. Figure 5 indicates that the domain boundary projected onto the yz or zx plane is directed with 68° from the y or x axis, while 44° in PMN-33PT,[6] and 69° in PMN-35PT.[8]

V. CONCLUSIONS

The domain structures of PZN-9PT with the MPB composition are observed at RT using scanning SHG microscopy. In the nonpoled sample, three types of domains, which are compatible with Pm symmetry, are observed at the surface. The direction of $\mathbf{P}_s$ is identified from the pattern of the SHG intensity distribution. $\mathbf{P}_s$ is found to be inclined at approximately 27° relative to the $[001]_c$ direction in the $(010)_c$ plane. The PolD of each domain is explained well by the corresponding theoretical formula.

Using the sample poled along the [101] direction, a 3D domain structure is obtained and consistent with Pm symmetry. The possible combination of two $\mathbf{P}_s$'s in adjacent domains is uniquely determined based on the Sapriel theory. It is concluded from this study that the macroscopic symmetry of PZN-9PT is monoclinic Pm including the orthorhombic phase located on the same Mc line at RT. This is the macroscopic symmetry averaged over the area determined by the optical diffraction limit. It should be stressed that the symmetry can be interpreted by the strain compatibility theory adopted in typical ferroelectrics. It is revealed that the PolD mapping can be a powerful technique for the analyses of domain structures and the spontaneous polarization directions of ferroelectric crystals.

ACKNOWLEDGMENTS

This research was partly supported by the "Academic Frontier" Project of MEXT. J. K. is grateful for the support of Grants-in-Aid for JSPS, Japan. The authors express their thanks to Y. Yamashita for providing PZN-9PT single crystals.

APPENDIX: POSSIBLE SHG TENSORS MATRICES CORRESPONDING TO 12 TYPES OF DOMAINS IN MONOCLINIC *Pm*

The third-rank polar i-tensor matrix $d^{(1)}$ of the monoclinic point group m is expressed as[31]

$$d^{(1)} = \begin{pmatrix} d_{11} & d_{12} & d_{13} & 0 & d_{15} & 0 \\ 0 & 0 & 0 & d_{24} & 0 & d_{26} \\ d_{31} & d_{32} & d_{33} & 0 & d_{35} & 0 \end{pmatrix}, \tag{A1}$$

where the y axis is chosen to be perpendicular to the mirror plane. This tensor matrix corresponds to the spontaneous polarization $\mathbf{P}_1$ in Table I. SHG tensor matrices $d^{(k)}$ with different $\mathbf{P}_k$ $(k=1,2,\ldots,12)$ are obtained by operating the transformation matrix. Results are listed as follows:

$$d^{(2)} = \begin{pmatrix} d_{33} & d_{32} & d_{31} & 0 & d_{35} & 0 \\ 0 & 0 & 0 & d_{26} & 0 & d_{24} \\ d_{13} & d_{12} & d_{11} & 0 & d_{15} & 0 \end{pmatrix}, \tag{A2}$$

$$d^{(3)} = \begin{pmatrix} d_{33} & d_{32} & d_{31} & 0 & -d_{35} & 0 \\ 0 & 0 & 0 & -d_{26} & 0 & d_{24} \\ -d_{13} & -d_{12} & -d_{11} & 0 & d_{15} & 0 \end{pmatrix}, \quad \text{(A3)}$$

$$d^{(4)} = \begin{pmatrix} -d_{11} & -d_{12} & -d_{13} & 0 & d_{15} & 0 \\ 0 & 0 & 0 & d_{24} & 0 & -d_{26} \\ d_{31} & d_{32} & d_{33} & 0 & -d_{35} & 0 \end{pmatrix}, \quad \text{(A4)}$$

$$d^{(5)} = \begin{pmatrix} d_{11} & d_{13} & d_{12} & 0 & 0 & -d_{15} \\ -d_{31} & -d_{33} & -d_{32} & 0 & 0 & d_{35} \\ 0 & 0 & 0 & -d_{24} & d_{26} & 0 \end{pmatrix}, \quad \text{(A5)}$$

$$d^{(6)} = \begin{pmatrix} d_{33} & d_{31} & d_{32} & 0 & 0 & -d_{35} \\ -d_{13} & -d_{11} & -d_{12} & 0 & 0 & d_{15} \\ 0 & 0 & 0 & -d_{26} & d_{24} & 0 \end{pmatrix}, \quad \text{(A6)}$$

$$d^{(7)} = \begin{pmatrix} d_{33} & d_{31} & d_{32} & 0 & 0 & d_{35} \\ d_{13} & d_{11} & d_{12} & 0 & 0 & d_{15} \\ 0 & 0 & 0 & d_{26} & d_{24} & 0 \end{pmatrix}, \quad \text{(A7)}$$

$$d^{(8)} = \begin{pmatrix} d_{11} & d_{13} & d_{12} & 0 & 0 & d_{15} \\ d_{31} & d_{33} & d_{32} & 0 & 0 & d_{35} \\ 0 & 0 & 0 & d_{24} & d_{26} & 0 \end{pmatrix}, \quad \text{(A8)}$$

$$d^{(9)} = \begin{pmatrix} 0 & 0 & 0 & 0 & -d_{26} & d_{24} \\ d_{32} & d_{33} & d_{31} & -d_{35} & 0 & 0 \\ -d_{12} & -d_{13} & -d_{11} & d_{15} & 0 & 0 \end{pmatrix}, \quad \text{(A9)}$$

$$d^{(10)} = \begin{pmatrix} 0 & 0 & 0 & 0 & -d_{26} & -d_{24} \\ -d_{32} & -d_{33} & -d_{31} & -d_{35} & 0 & 0 \\ -d_{12} & -d_{13} & -d_{11} & -d_{15} & 0 & 0 \end{pmatrix}, \quad \text{(A10)}$$

$$d^{(11)} = \begin{pmatrix} 0 & 0 & 0 & 0 & d_{24} & d_{26} \\ d_{12} & d_{11} & d_{13} & d_{15} & 0 & 0 \\ d_{32} & d_{31} & d_{33} & d_{35} & 0 & 0 \end{pmatrix}, \quad \text{(A11)}$$

$$d^{(12)} = \begin{pmatrix} 0 & 0 & 0 & 0 & d_{24} & -d_{26} \\ -d_{12} & -d_{11} & -d_{13} & d_{15} & 0 & 0 \\ d_{32} & d_{31} & d_{33} & -d_{35} & 0 & 0 \end{pmatrix}. \quad \text{(A12)}$$

When the observed plane is the zx plane as in the present experiment, the components related to the y component of light-polarization can be neglected, and the polarization dependence of SHG intensity is expressed by Eq. (3)–(5).

*grand-lethal@y.suou.waseda.jp
†uesu93@waseda.jp

[1] Y. Yamada, T. Iwase, K. Fujishiro, Y. Uesu, Y. Yamashita, I. Tomeno, and S. Shimanuki, Ferroelectrics **240**, 1629 (2000).
[2] G. Burns and F. H. Dacol, Phys. Rev. B **28**, 2527 (1983).
[3] K. Fujishiro, R. Vlokh, Y. Uesu, Y. Yamada, J.-M. Kiat, B. Dkhil, and Y. Yamashita, Jpn. J. Appl. Phys., Part 1 **37**, 5246 (1998).
[4] B. Noheda, D. E. Cox, G. Shirane, J. A. Gonzalo, L. E. Cross, and S.-E. Park, Appl. Phys. Lett. **74**, 2059 (1999).
[5] H. Fu and R. E. Cohen, Nature (London) **403**, 281 (2000).
[6] A. A. Bokov and Z.-G. Ye, J. Appl. Phys. **95**, 6347 (2004).
[7] Y. Uesu, M. Matsuda, Y. Yamada, K. Fujishiro, D. E. Cox, B. Noheda, and G. Shirane, J. Phys. Soc. Jpn. **71**, 960 (2002).
[8] J.-M. Kiat, Y. Uesu, B. Dkhil, M. Matsuda, C. Malibert, and G. Calvarin, Phys. Rev. B **65**, 064106 (2002).
[9] M. Iwata, T. Araki, M. Maeda, I. Suzuki, H. Ohwa, N. Yasuda, H. Orihara, and Y. Ishibashi, Jpn. J. Appl. Phys., Part 1 **41**, 7003 (2002).
[10] W. S. Chang, L. C. Lim, P. Yang, C.-M. Hsieh, and C.-S. Tu, J. Phys.: Condens. Matter **20**, 445218 (2008).
[11] W. S. Chang, L. C. Lim, P. Yang, H. Miao, C.-S. Tu, Q. Chen, and A. K. Soh, Appl. Phys. Lett. **94**, 202907 (2009).
[12] S. Wada, S.-E. Park, L. E. Cross, and T. R. Shrout, Ferroelectrics **221**, 147 (1999).
[13] S. Madeswaran, S. V. Rajasekaran, R. Jayavel, S. Ganesamoorthy, and G. Behr, Mater. Sci. Eng., B **120**, 32 (2005).
[14] G. Singh, I. Bhaumik, S. Ganesamoorthy, A. K. Karnal, and V. S. Tiwari, Cryst. Res. Technol. **42**, 378 (2007).
[15] J. Sapriel, Phys. Rev. B **12**, 5128 (1975).
[16] V. Gopalan and R. Raj, J. Appl. Phys. **81**, 865 (1997).
[17] E. D. Mishina, N. E. Sherstyuk, D. R. Barskiy, A. S. Sigov, Yu. I. Golovko, V. M. Mukhorotov, M. De Santo, and Th. Rasing, J. Appl. Phys. **93**, 6216 (2003).
[18] K. A. Schönau, M. Knapp, H. Kungl, M. J. Hoffmann, and H. Fuess, Phys. Rev. B **76**, 144112 (2007).
[19] D. La-Orauttapong, B. Noheda, Z.-G. Ye, P. M. Gehring, J. Toulouse, D. E. Cox, and G. Shirane, Phys. Rev. B **65**, 144101 (2002).
[20] J. Kaneshiro, S. Kawado, H. Yokota, Y. Uesu, and T. Fukui, J. Appl. Phys. **104**, 054112 (2008).
[21] C.-S. Tu, F. –T. Wang, R. R. Chien, V. H. Schmidt, and L.-C. Lim, J. Appl. Phys. **100**, 074105 (2006).
[22] J. Kaneshiro, Y. Uesu, and T. Fukui, Jpn. J. Appl. Phys. **48**, 09KF09 (2009).
[23] E. K. H. Salje, *Phase Transitions in Ferroelastic and Coelastic Crystals* (Cambridge University Press, Cambridge, 1990).
[24] Y. Uesu, S. Kurimura, and Y. Yamamoto, Appl. Phys. Lett. **66**, 2165 (1995).
[25] S. Kurimura and Y. Uesu, J. Appl. Phys. **81**, 369 (1997).
[26] J. Kaneshiro, Y. Uesu, and T. Fukui, J. Opt. Soc. Am. B **27**, 888 (2010).
[27] B. Noheda, Z. Zhong, D. E. Cox, G. Shirane, S.-E. Park, and P. Rehrig, Phys. Rev. B **65**, 224101 (2002).

[28] D. E. Cox, B. Noheda, G. Shirane, Y. Uesu, K. Fujishiro, and Y. Yamada, Appl. Phys. Lett. **79**, 400 (2001).
[29] B. Noheda, D. E. Cox, G. Shirane, S.-E. Park, L. E. Cross, and Z. Zhong, Phys. Rev. Lett. **86**, 3891 (2001).
[30] D. Viehland, J. Appl. Phys. **88**, 4794 (2000).
[31] J. F. Nye, *Physical Properties of Crystals* (Oxford University Press, Oxford, 1957).